Manipulating propagating graphene plasmons at near field by shaped graphene nano-vacancies

Du, Luping; Tang, Dingyuan

2014

Du, L., & Tang, D. (2014). Manipulating propagating graphene plasmons at near field by shaped graphene nano-vacancies. Journal of the Optical Society of America A, 31(4), 691-695.

https://hdl.handle.net/10356/104119

https://doi.org/10.1364/JOSAA.31.000691

Manipulating propagating graphene plasmons at near field by shaped graphene nano-vacancies

Luping Du and Dingyuan Tang*

School of Electrical & Electronic Engineering, Nanyang Technological University, Nanyang Avenue, Singapore 639798
**Corresponding author: edytang@ntu.edu.sg*

Received November 12, 2013; revised January 26, 2014; accepted January 28, 2014;
posted January 29, 2014 (Doc. ID 201207); published March 11, 2014

Surface plasmons in graphene have many promising properties, such as high confinement, low losses, and gate-tunability. However, it is also the high confinement that makes them difficult to excite due to their large momentum mismatch with free-space mid-infrared light. We propose to use shaped graphene nano-vacancies to compensate for the momentum mismatch, revealing its high flexibility in graphene plasmon (GP) excitation and manipulation. We first examine the electromagnetic standing waves generated with a pair of straight vacancies, in order to verify the excitation of GPs and to illustrate their tunability with gate voltage. Plasmonic lenses are then designed to achieve the super-focusing of mid-infrared light and to generate plasmonic vortices in graphene. A $\sim 0.0125\lambda_0$ hotspot is generated, far below the optical diffraction limit, hence revealing the capability of light control at deep-subwavelength scale.

OCIS codes: (240.6680) Surface plasmons; (130.3060) Infrared; (220.3630) Lenses; (080.4865) Optical vortices.
http://dx.doi.org/10.1364/JOSAA.31.000691

1. INTRODUCTION

Control of light at deep-subwavelength scale is an arduous though crucial task for achieving miniaturized integrated photonic circuits. Methods involving surface plasmons (SPs) [1–3], the electromagnetic waves strongly bound to a conductor surface, are considered to be the most effective. The conventional materials of choice used to support SPs are noble metals, such as gold and silver. However, SPs generated on a smooth noble metal surface often suffer from high losses together with a relatively low degree of localization (plasmon wavelength λ_{sp} is close to its free-space wavelength λ_0). Both of them limit greatly the effectiveness of light confinement at deep-subwavelength scale.

Graphene [4,5], a single two-dimensional form of carbon atoms arranged in a honeycomb lattice, has drawn a great amount of interest in nanophotonics recently because it was found that the strongly confined SP mode can exist in graphene at mid-infrared frequencies due to its high carrier mobility at room temperature and under high carrier density [6–11]. The degree of localization, quantified as λ_0/λ_{sp}, can reach several tens [6]. It is much higher than that of the propagating SP mode supported on a smooth metal surface [2]. Meanwhile, the mode losses can be much smaller, which means a longer lifetime of SPs in terms of plasmon wavelength [6]. Moreover, the carrier density in graphene, which determines its electronic Fermi energy level, can be adjusted effectively with a small bias voltage applied on a field-effect transistor [12]. The Fermi energy level influences directly the dispersion relation of SPs in graphene, hence leading to a broadband tunability of graphene plasmons (GPs).

While the properties of high confinement, low losses, and gate-tunability of GP make graphene a promising material for the subwavelength control of light, the excitation of GPs is difficult because of the larger momentum mismatch between the GPs and free-space light (e.g., $q_{sp}/q_0 \approx 42$ for GP at 8 μm, where q represents the wavenumber). One approach is to use a sharp tip as done in [7,8]. By focusing a mid-infrared incident light onto the tip just above graphene, a wide momenta range up to a few times $1/a$ (a is the curvature radius of the tip) is induced, which covers the typical range of GPs at mid-infrared frequencies and hence enables phase-matching excitation of GPs. Owing to the dual function of the sharp tip (excitation and collection), the near-field SPs in graphene were uncovered experimentally for the first time. But from the perspective of plasmon excitation, such a configuration lacks flexibility and hence limits its application. A more common approach is using gratings as the momentum generator, including the graphene ribbon array [12–16] and diffractive dielectric gratings [17–19]. Both configurations are able to excite efficiently the infrared GPs, but they mainly employ the far-field properties of SPs, such as transmission dips under resonance conditions, while the near-field SPs cannot be manipulated easily with periodic structures.

In this paper, we present flexible plasmon generators by using shaped graphene nano-vacancies. Similar to the tip configuration, a wide range of momentum is induced from the strong interaction between light and graphene edges, which covers those of mid-infrared GPs. Nevertheless, the vacancy approach has a much higher degree of flexibility that enables tunable generation and manipulation of GPs with designed plasmonic structures. As demonstrations, we first investigate the GP standing waves generated with a pair of straight vacancies in order to, on the one hand, verify the excitation of GPs, and, on the other hand, illustrate their tunability through gate voltage. We then design plasmonic lenses to realize the super-focusing of mid-infrared light via GPs and to generate the plasmonic vortices in graphene. Throughout the paper, finite-difference time-domain (FDTD) simulation

was carried out to study the near-field properties of SPs in graphene.

2. VERIFICATION OF GRAPHENE PLASMON EXCITATION WITH NANO-VACANCY

SPs in graphene are the transverse magnetic (TM) eigenmodes that satisfy the Maxwell equations when graphene is sandwiched between two dielectric layers. Their dispersion relationship at the nonretarded regime can be expressed as [6]

$$q = \frac{\varepsilon_0(\varepsilon_1+\varepsilon_2)}{2}\frac{2i\omega}{\sigma(\omega,q)}, \tag{1}$$

where ε_1 and ε_2 are the permittivities of dielectrics above and below graphene, σ is the conductivity of graphene, ω the incident frequency, and q is the wavenumber of GP. At the mid-infrared region, optical losses from interband transition and phonons can be neglected for a properly doped graphene and hence the conductivity σ can simply be described with the Drude model as [6]

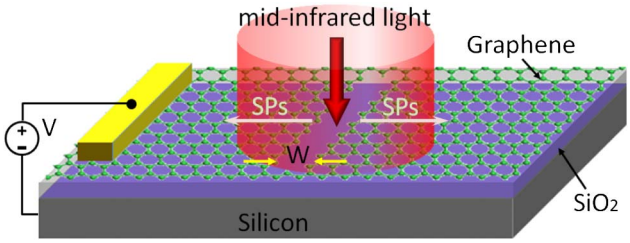

Fig. 1. Schematic diagram of SP generation in graphene with a single straight graphene vacancy.

$$\sigma(\omega) = \frac{e^2E_f}{\pi\hbar^2}\frac{i}{\omega+i\tau^{-1}}. \tag{2}$$

E_f represents the electronic Fermi energy (or chemical potential) of graphene, which relates with its carrier density n as $E_f = \hbar v_f(\pi n)^{1/2}$, where v_f is the Fermi velocity in graphene. E_f can be adjusted electrically with gate voltage or chemically with doping. τ describes the relaxation time of charges in graphene, which is determined by the carrier mobility μ in graphene as $\tau = \mu E_f/ev_f^2$.

Typically, the wavenumber q of GP is much larger than that of free-space light (ω_0/c) and hence a wave-vector generator is required to compensate for their momentum mismatch. Figure 1 shows the schematic diagram of GP excitation with a straight graphene vacancy. A wide range of in-plane wavevector is induced when a mid-infrared light polarized perpendicular to the vacancy is illuminated onto graphene, which includes that of GP. Hence, GPs are excited from the vacancy and propagate to the two lateral sides. To verify the excitation of GP, we numerically model the system, which includes a pair of straight vacancies, as shown in Fig. 2(a). Under this circumstance, a GP standing wave will be generated between the vacancies, from which plasmon wavelength can be extracted and compared with the theoretical one from Eq. (1).

In the simulations, the permittivity of graphene, which determines its optical properties, is derived from its conductivity σ with $\varepsilon_{\text{gra}} = 2.5 + i\sigma/\varepsilon_0\omega t$, where t is the thickness of graphene [17]. Throughout the paper we used a nonphysical value of 1 nm because the result (near-field pattern) is independent on t. It is worthwhile to mention that although graphene is an anisotropic material [17,20], we treated it as isotropic in our work, as the out-of-plane permittivity gives rise to a tiny influence on the simulation result. For the conductivity of graphene, as many previous works did, we

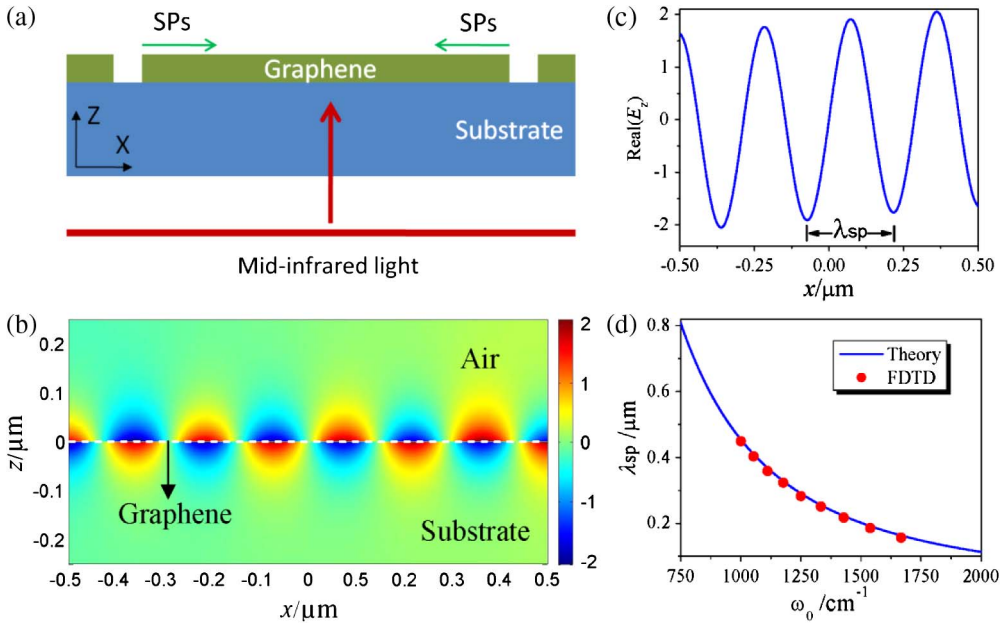

Fig. 2. Verification of SP generation in graphene by a pair of straight graphene vacancies. (a) Schematic diagram of the excitation configuration. (b) Snapshot of E_z component during calculation, clearly showing an electromagnetic standing wave and the strong confinement of the electric field near graphene. (c) Cross-section distribution of real (E_z) 5 nm above graphene from (b). The pitch (i.e., the SP wavelength) of the standing wave is 284 nm, in line well with the value predicted from theory (290 nm). (d) Obtained dispersion relation from a wavelength sweep (circles), according excellently with the dispersion curve (solid line) calculated with Eq. (1).

assumed a moderate mobility of $10,000\ \mathrm{cm}^2/(\mathrm{V}\cdot\mathrm{s})$ and that E_f is 0.64 eV. This corresponds to a relaxation time of 0.64 ps. ε_1 and ε_2 are 1.0 and 2.25, respectively, corresponding to air and the substrate. The width of each vacancy is 240 nm, and their separation is 3 μm.

Figure 2(b) shows a snapshot of the E_z component during the calculation at an incident wavelength of 8 μm. On the one hand, the electric field is strongly confined in the vicinity of graphene. The decaying length along the vertical direction is measured at only 24 nm. It is ~1 order of magnitude smaller than that of SPs on a metal surface [1]. On the other hand, a standing wave is generated between the vacancies. From the cross-section distribution 5 nm above the graphene [Fig. 2(c)], the pitch of the standing wave (i.e., the SP wavelength) is 284 nm. This is very close to the value predicted from Eq. (1) (290 nm). We further carried out a wavelength sweep and obtained each plasmon wavelength. The result is shown in Fig. 2(d) with red circles, together with the theoretical curve from Eq. (1). We can see a good match between FDTD and theory, hence unambiguously verifying the excitation of GPs with the graphene vacancies.

The pitch of the standing wave can effectively and conveniently be tuned with a bias voltage applied on a field-effect transistor by changing the Fermi energy of graphene, as illustrated in Fig. 1. For simplicity, we ignore the connection between E_f and gate voltage, but only assume a small change of E_f in the simulation. From Eq. (1), the Fermi energy influences directly the dispersion relation of GP. Figure 3(a) shows a series of dispersion curves when E_f is increased from 0.4 to 0.9 eV, with a 0.1 eV increment. At a fixed wavelength, the GP wavelength is red-shifted with an increment of Fermi energy. The FDTD simulation results are shown in Fig. 3(b), in which the pitch of the standing wave is increased linearly when raising the Fermi energy. The linearity between GP wavelength and E_f is further verified analytically [inset in Fig. 3(a)] and can be directly seen in Eq. (1) ($q = 2\pi/\lambda_{\mathrm{sp}}$). Such linearity is an important property of GPs and may find applications in tunable nanolithography and super-resolved imaging [21].

3. SUPER-FOCUSING OF MID-INFRARED LIGHT VIA GRAPHENE PLASMONS

Benefiting from the flexible excitation of GPs with nanovacancy, SPs in graphene can be manipulated conveniently with designed nanostructures. As the first demonstration, we present a spiral-shaped vacancy that can achieve the focusing of mid-infrared light at deep-subwavelength scale. A schematic diagram of the excitation configuration and the specifications of the structure are shown in Figs. 4(a) and 4(b), respectively. As can be seen from Fig. 4(b), the radius of the vacancy is increased linearly from R to $R + \lambda_{\mathrm{SP}}$ along the azimuthal direction. As a mid-infrared incident light illuminates onto the structure, GPs will be excited from all azimuthal directions with the vacancy and the linear distance discrepancy will be transferred to the initial phase delay of GPs linked by $\Delta\varphi = 2\pi\cdot\Delta r/\lambda_{\mathrm{SP}}$. In other words, the spiral structure produces a linear phase delay of GPs equal to $l\cdot\varphi$ (here $l = 1$), where l is termed as the topological charge of the structure and φ denotes the azimuthal angle.

Figure 4(c) is the FDTD modeling result, showing the amplitude of the E_z component 5 nm above graphene. In

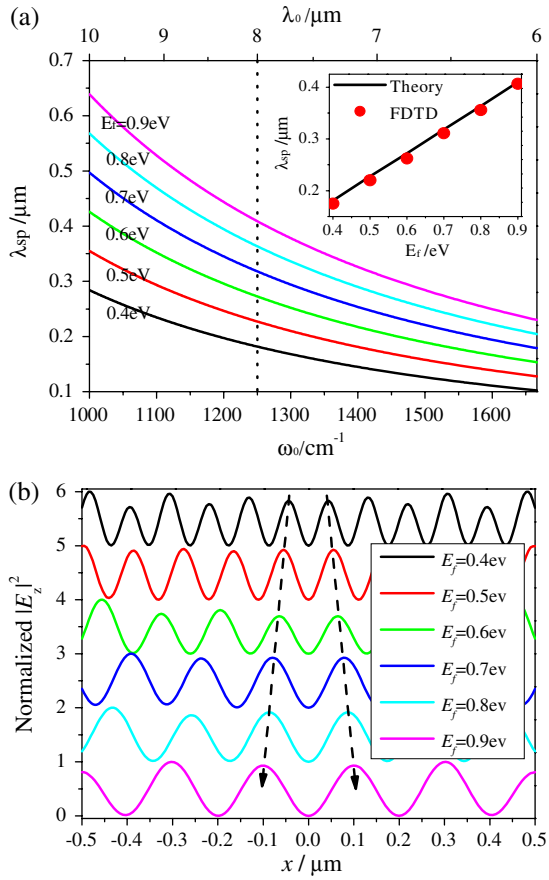

Fig. 3. Gate-tuning of GPs. (a) Dispersion curves at various Fermi energies obtained with Eq. (1). The inset plots the relationship between plasmon wavelength and Fermi energy at a fixed incident wavelength of 8 μm, showing linearity between them. The FDTD data are derived from (b). (b) Series of SP standing waves between the two vacancies at various Fermi energies as shown in Fig. 2(a).

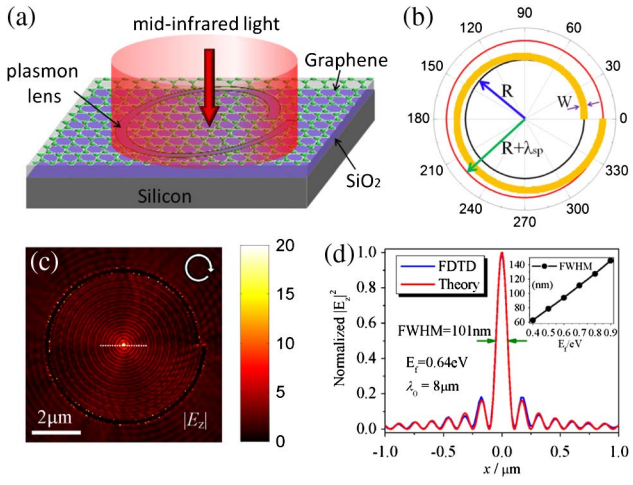

Fig. 4. Super-focusing of mid-infrared light via GPs by using a spiral-shaped graphene vacancy together with a circularly polarized incident beam. (a) Excitation scheme. (b) Specification of the designed spiral vacancy. (c) FDTD simulation result, showing the amplitude of E_z component 5 nm above graphene. A hotspot is generated at the geometric center. (d) Cross-section distribution along the white dashed line in (c) as compared with the analytical one obtained with Eq. (3). The size of hotspot is measured to be 101 nm, ~$0.0125\lambda_0$ in terms of incident wavelength. The inset shows the dependence of hotspot size on the Fermi energy of graphene.

the simulation, the base radius R of the vacancy is set to be 3 μm, λ_{SP} is 284 nm corresponding to the 8 μm incident wavelength, the width of vacancy is 240 nm, and the incident beam is left-hand circularly polarized. As can be seen from Fig. 4(c), a strongly confined hotspot is formed at the geometric center encircled by a concentric standing wave because of the interference of GPs from all directions. From the cross-section distribution along the dashed white line, the size of the hotspot [in terms of full width at half-maximum (FWHM)] is measured to be 101 nm. In terms of incident wavelength, it is $\sim 0.0125\lambda_0$, far below the optical diffraction limit ($0.5\lambda_0$) and the limitation making use of conventional propagating SPs on a smooth metal surface ($\sim 0.35\lambda_0$) [22].

Mathematically, on the one hand, the spiral-shaped vacancy can be treated as infinite numbers of point sources of GPs, of which the initial phase delay with respect to the inner circle [the black one as shown in Fig. 4(b)] is $l \cdot \varphi$, as analyzed above. On the other hand, only the polarization perpendicular to the vacancy can excite SPs, i.e., the radial component of incident light for a ring structure. For a circular polarization, the John's vector defined in the $r\varphi$ coordinate system is $\exp(\pm i\varphi)[1, \pm i]$. Thus, the near-field intensity within the inner circle can be represented as a summation of the contributions from all of the point sources as

$$E_z \propto \int_0^{2\pi} \exp(im\varphi)\exp(il\varphi)\exp[ik_{SP}(x\cos\varphi + y\sin\varphi)]d\varphi = 2\pi J_{(m+l)}(k_{SP}r)\exp[i(m+l)(\varphi+\pi/2)], \quad (3)$$

where $m \cdot \varphi$ denotes the phase structure of incident light, l the topological charge of the structure, and J_{m+l} the first kind Bessel function with order $m + l$. In our simulation, $m = -1$, corresponding to the left-hand circularly polarized light. Hence, the intensity of SPs can be described by the zero-order Bessel function. The normalized intensity distribution obtained with Eq. (3) is plotted in Fig. 4(d), according excellently with the FDTD result.

From Eq. (3), the same intensity pattern could be obtained when both m and l are equal to zero, i.e., a radially polarized light [23] ($m = 0$) illuminates onto a ring structure ($l = 0$). Practically, such a combination may induce difficulty in alignment between incident light and structure because of the donut shape of a radially polarized light. However, because the structure in this case is independent on λ_{SP} (hence on E_f), it will benefit from the tunability of GPs; i.e., the size of the hotspot can be tuned conveniently with gate voltage. The inset in Fig. 4(d) shows the dependence of the hotspot size on the Fermi energy of graphene at an incident wavelength of 8 μm. The hotspot can further be shrunk greatly by lowering the Fermi energy, even reaching several tens of nanometers. In terms of incident wavelength, GP can focus a free-space light into a spot 1–2 orders of magnitude smaller than that by using conventional optical components (lens) or SPs on a smooth metal surface. Such super-focusing capability together with gate-tunability makes it attractive in applications such as super-resolved imaging.

4. PLASMONIC VORTEX GENERATION AT GRAPHENE

If the topological charge of the structure in Fig. 4(b) is greater than 1, a plasmonic vortex will be generated in graphene [24].

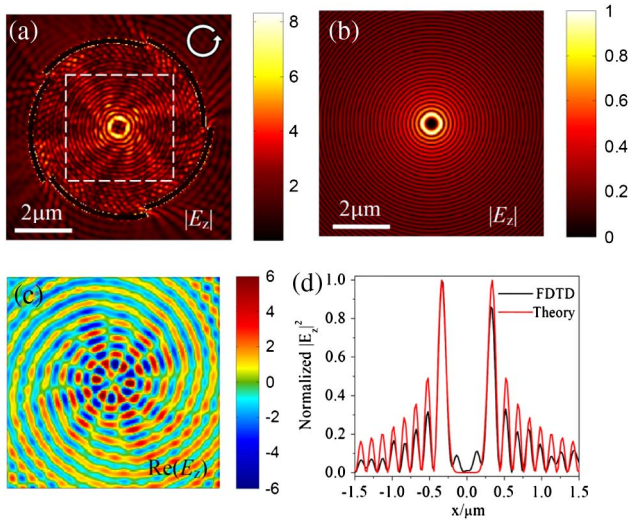

Fig. 5. Generation of plasmonic vortices at graphene. (a) Amplitude distribution of E_z component 5 nm above graphene obtained with FDTD, when the topological charge of vacancy is 5 together with a right-handed circular polarization. (b) Normalized E_z distribution from Eq. (3) assuming $l = 5$ and $m = 1$. (c) Snapshot of the real part of the E_z component during calculation, showing the evolution of the plasmonic vortex. (d) Cross-section comparison between (a) and (b), which presents a good agreement.

Under this circumstance, from Eq. (3), the GP profile after interference possesses a spiral phase equal to $(m + l) \cdot \varphi$, where $m + l \neq 0$. Thus, its intensity is related with a high-order Bessel function, which has zero intensity at the center because of the phase singularity.

In Fig. 5 we show the simulated and calculated plasmonic vortex when l and m are equal to 5 and 1 (right-hand circularly polarized light), respectively. The structure can be seen in Fig. 5(a), which has five separated segments with each producing a 0–2π phase increment. As predicted, the intensity profile is dark at the center owing to the phase singularity, which is encompassed by a bright ring termed as the primary ring of a plasmonic vortex. Outside the primary ring is an SP standing wave with pitch equal to $\lambda_{SP}/2$. It is noted that outside the structure there are also interference fringes [they can also be seen in Fig. 4(c)]. These should attribute to the interference between SPs and the incident plane-wave because the fringe separation is λ_{SP}.

For comparison, Fig. 5(b) shows the normalized amplitude distribution of the electric field from Eq. (3) when $l = 5$ and $m = 1$. The positions of each fringe agree well with each other from their cross-section distributions across the center as can be seen in Fig. 5(d). Figure 5(c) gives a snapshot of the real part of the E_z component during the calculation at the central area as defined in Fig. 5(a) with a dashed square, clearly showing the formation process of the plasmonic vortex. Although the topological charge of the structure is 5, the number of spiral arms of SPs in Fig. 5(c) is 6, with the additional one coming from the spin of circularly polarized light. Also at the center the number of node is 6. Both of them indicate that the topological charge of the generated plasmonic vortex is 6. Thus, by changing the topological charge of the structure or phase structure of incident light, the near-field properties of the plasmonic vortex can easily be tuned.

5. CONCLUSION

In this paper, we propose to use the nano-scale vacancy of graphene for the excitation of GPs. Benefiting from the flexibility of the vacancy configuration, SPs in graphene can be manipulated at the near field in an arbitrary way. We first studied the GP standing waves generated with a pair of straight vacancies. The dispersion relationship extracted from the standing waves accords well with the analytical one, hence verifying the excitation of GPs. Meanwhile, we demonstrated that the pitch of the standing wave can be tuned conveniently owing to the gate-tunability of GPs. We then designed a spiral-shaped graphene vacancy to achieve the super-focusing of mid-infrared light. $A \sim 0.0125\lambda_0$ hotspot is achieved numerically, far below the optical diffraction limit. Moreover, the size of hotspot can be tuned with gate voltage and can further be down to tens of nanometers. We finally demonstrate the generation of plasmonic vortices at graphene. The topological charge of the generated GP vortex comes from both the structure and spin of incident light, hence with great tunability. We believe that the flexible excitation and manipulation of GPs with shaped nano-vacancies will accelerate the exploration of SPs in graphene at the near field and shed light on the plasmonic applications, such as miniaturized photonics circuits, nano-lithography, and super-resolution imaging.

ACKNOWLEDGMENTS

This work was supported by the Minister of Education (MOE) Singapore under Grant No. 35/12.

REFERENCES

1. W. L. Barnes, A. Dereux, and T. W. Ebbesen, "Surface plasmon subwavelength optics," Nature **424**, 824–830 (2003).
2. S. Maier, *Plasmonics: Fundamentals and Applications* (Springer, 2007).
3. J. B. Pendry, A. Aubry, D. R. Smith, and S. A. Maier, "Transformation optics and subwavelength control of light," Science **337**, 549–552 (2012).
4. A. K. Geim and K. S. Novoselov, "The rise of graphene," Nat. Mater. **6**, 183–191 (2007).
5. K. S. Novoselov, V. I. Fal'ko, L. Colombo, P. R. Gellert, M. G. Schwab, and K. Kim, "A roadmap for graphene," Nature **490**, 192–200 (2012).
6. M. Jablan, H. Buljan, and M. Soljacic, "Plasmonics in graphene at infrared frequencies," Phys. Rev. B **80**, 245435 (2009).
7. J. N. Chen, M. Badioli, P. Alonso-Gonzalez, S. Thongrattanasiri, F. Huth, J. Osmond, M. Spasenovic, A. Centeno, A. Pesquera, P. Godignon, A. Z. Elorza, N. Camara, F. J. G. de Abajo, R. Hillenbrand, and F. H. L. Koppens, "Optical nano-imaging of gate-tunable graphene plasmons," Nature **487**, 77–81 (2012).
8. Z. Fei, A. S. Rodin, G. O. Andreev, W. Bao, A. S. McLeod, M. Wagner, L. M. Zhang, Z. Zhao, M. Thiemens, G. Dominguez, M. M. Fogler, A. H. C. Neto, C. N. Lau, F. Keilmann, and D. N. Basov, "Gate-tuning of graphene plasmons revealed by infrared nano-imaging," Nature **487**, 82–85 (2012).
9. A. N. Grigorenko, M. Polini, and K. S. Novoselov, "Graphene plasmonics," Nat. Photonics **6**, 749–758 (2012).
10. Q. L. Bao and K. P. Loh, "Graphene photonics, plasmonics, and broadband optoelectronic devices," ACS Nano **6**, 3677–3694 (2012).
11. A. Vakil and N. Engheta, "Transformation optics using graphene," Science **332**, 1291–1294 (2011).
12. L. Ju, B. S. Geng, J. Horng, C. Girit, M. Martin, Z. Hao, H. A. Bechtel, X. G. Liang, A. Zettl, Y. R. Shen, and F. Wang, "Graphene plasmonics for tunable terahertz metamaterials," Nat. Nanotechnol. **6**, 630–634 (2011).
13. H. G. Yan, T. Low, W. J. Zhu, Y. Q. Wu, M. Freitag, X. S. Li, F. Guinea, P. Avouris, and F. N. Xia, "Damping pathways of mid-infrared plasmons in graphene nanostructures," Nat. Photonics **7**, 394–399 (2013).
14. A. Y. Nikitin, F. Guinea, F. J. Garcia-Vidal, and L. Martin-Moreno, "Surface plasmon enhanced absorption and suppressed transmission in periodic arrays of graphene ribbons," Phys. Rev. B **85**, 081405(R) (2012).
15. B. Wang, X. Zhang, F. J. Garcia-Vidal, X. C. Yuan, and J. Teng, "Strong coupling of surface plasmon polaritons in monolayer graphene sheet arrays," Phys. Rev. Lett. **109**, 073901 (2012).
16. V. V. Popov, T. Y. Bagaeva, T. Otsuji, and V. Ryzhii, "Oblique terahertz plasmons in graphene nanoribbon arrays," Phys. Rev. B **81**, 073404 (2010).
17. W. L. Gao, J. Shu, C. Y. Qiu, and Q. F. Xu, "Excitation of plasmonic waves in graphene by guided-mode resonances," ACS Nano **6**, 7806–7813 (2012).
18. W. Gao, G. Shi, Z. Jin, J. Shu, Q. Zhang, R. Vajtai, P. M. Ajayan, J. Kono, and Q. Xu, "Excitation and active control of propagating surface plasmon polaritons in graphene," Nano Lett. **13**, 3698–3702 (2013).
19. X. L. Zhu, W. Yan, P. U. Jepsen, O. Hansen, N. A. Mortensen, and S. S. Xiao, "Experimental observation of plasmons in a graphene monolayer resting on a two-dimensional subwavelength silicon grating," Appl. Phys. Lett. **102**, 131101 (2013).
20. V. G. Kravets, A. N. Grigorenko, R. R. Nair, P. Blake, S. Anissimova, K. S. Novoselov, and A. K. Geim, "Spectroscopic ellipsometry of graphene and an exciton-shifted van Hove peak in absorption," Phys. Rev. B **81**, 155413 (2010).
21. Q. Wang, J. Bu, P. S. Tan, G. H. Yuan, J. H. Teng, H. Wang, and X. C. Yuan, "Subwavelength-sized plasmonic structures for wide-field optical microscopic imaging with super-resolution," Plasmonics **7**, 427–433 (2012).
22. L. Du, D. Y. Lei, G. Yuan, H. Fang, X. Zhang, Q. Wang, D. Tang, C. Min, S. A. Maier, and X. Yuan, "Mapping plasmonic near-field profiles and interferences by surface-enhanced Raman scattering," Sci. Rep. **3**, 3064 (2013).
23. L. P. Du, G. H. Yuan, D. Y. Tang, and X. C. Yuan, "Tightly focused radially polarized beam for propagating surface plasmon-assisted gap-mode Raman spectroscopy," Plasmonics **6**, 651–657 (2011).
24. H. Kim, J. Park, S. W. Cho, S. Y. Lee, M. Kang, and B. Lee, "Synthesis and dynamic switching of surface plasmon vortices with plasmonic vortex lens," Nano Lett. **10**, 529–536 (2010).